Journal of Engineering, Project, and Production Management
2026, 16(5), 2025-229

Optimization of Automotive Aerodynamic Appearance Design Using an Improved EGO Algorithm

Zhonghua Zhao[1] and Zhibin Qiu[2]
[1] Professor, School of Art and Design, Anhui Business and Technology College, Hefei, 230041, China, E-mail: zhao.zh1982@outlook.com (corresponding author).
[2] Associate Professor, School of Art and Design, Anhui Business and Technology College, Hefei, 230041, China.

Engineering Management
Received October 14, 2025; revised December 29, 2025; accepted January 29, 2026
Available online June 17, 2026

Abstract: Traditional automotive aerodynamic exterior design relies on a large number of physical model tests, which are not only time-consuming and costly but also easily limited by experimental conditions and measurement accuracy. This research aims to improve the aerodynamic performance of automobiles by developing an efficient global optimization algorithm. The Kriging model is added to optimize the prediction performance, and the quasi Newton algorithm is integrated to seek the optimal appearance parameters that meet the requirements. Finally, the algorithm's performance is verified through both virtual and actual operations. The research outcomes reveal that the new algorithm has a fast convergence speed, and the drag coefficient stabilizes at 0.364~0.357 when the number of iterations reaches 400. The optimized car's drag coefficient decreases by an average of 36.89%. The new algorithm has high prediction accuracy, with a maximum prediction error of 2.1%. The new algorithm reduces resistance at the front of the vehicle by 1.65% and resistance at the sunroof by 44.56%. The fuel consumption per 100 kilometers of the car optimized by the new algorithm at 60 km/h is 8.96 L, which is 6.69% lower than that of the traditional efficient global optimization algorithm. From this, it can be seen that optimizing the aerodynamic appearance of automobiles through improved, efficient global optimization algorithms can significantly reduce the difficulty of vehicle exterior design, lower the vehicle's resistance in all directions, and provide a new method for reducing automobile energy consumption.

Keywords: Aerodynamic optimization, efficient global optimization, kriging surrogate model, vehicle design, drag reduction.

DOI 10.32738/JEPPM-2025-229

1. Introduction

In the modern automotive industry, the aerodynamic performance of a car not only directly affects its fuel economy and driving stability but also relates to environmental performance and driving experience (Nainggolan et al., 2024). With the increasing global emphasis on energy conservation, emissions reduction, and efficient transportation, optimizing the aerodynamic design of automobiles has become increasingly important in automotive design and exploration and development (Amirkhani et al., 2024). The application of computer algorithms has brought revolutionary changes to aerodynamic appearance optimization, greatly raising the validity and precision of design. In the process of aerodynamic appearance optimization, computer algorithms simulate the flow field characteristics for different designs by varying the exterior design parameters of the car, such as body lines, surface shapes, and front and rear spoilers (Lizarribar et al., 2024). The numerical model calculates key indicators, such as the car's air resistance and lift coefficients, providing strong data support for aerodynamic shape optimization. Many researchers have studied various approaches to improve automobile performance through aerodynamic appearance optimization. Xia et al. (2024) combined precise Computational Fluid Dynamics (CFD) simulations with empirical wind-tunnel tests to carefully analyze the direct impact of design changes on vehicle aerodynamic performance, aiming to improve driving efficiency. This method effectively verifies the accuracy of simulation predictions. Liu et al. (2024) proposed a structural optimization scheme to address excessive intake resistance in engine air filters. The results indicate that the optimized air filter has improved airflow velocity uniformity and significantly reduced intake resistance. Liu (2024) developed a vehicle energy consumption recognition model based on an improved recursive least squares algorithm and a neural network to predict and optimize electric vehicle energy consumption. This method can accurately predict vehicle energy consumption and reveal the energy utilization patterns of electric vehicles.

In terms of improving Efficient Global Optimization (EGO) algorithms. Huynh et al. (2024) proposed an EGO based on the Balancing Composite Motion Optimization (BCMO) algorithm to optimize the parameters of each unit device in order to improve the performance of hybrid electric vehicles. The results indicate that this method can accurately analyze the impact of various parameters on vehicle energy consumption. Wang (2025) introduced a novel heuristic optimization technique, the Draco Lizard Optimizer (DLO), to address a series of issues arising from the complexity of EGO. The results indicate that the method has excellent global search performance. The experiment outcomes verified the effectiveness and robustness of the new method, reduced computational costs, and achieved ideal aerodynamic optimization results. In summary, current research on optimizing automotive exterior aerodynamic design primarily focuses on reducing drag through modeling experiments or on improving algorithms to enhance computational performance. Scholars have not used a combination of algorithms and modeling methods to optimize exterior design for automotive aerodynamic performance. Based on this, an improved global optimization algorithm is developed. This research extends the EGO algorithm by integrating Kriging prediction refinement with quasi-Newton convergence acceleration to achieve faster convergence and higher prediction accuracy. To reduce air resistance at high speeds, an innovative Kriging surrogate model is used to optimize the aerodynamic shape. To handle multidimensional optimization problems efficiently and stably, the quasi Newton method is integrated to reduce the surrogate model's error. Finally, a wind tunnel model is set to verify the aerodynamic appearance performance parameters.

2. Methods

2.1. Improved EGO Algorithm

With the urgent need to improve the fuel economy of automobiles and reduce environmental impact, in-depth research and optimization of the aerodynamic design of automobiles to effectively reduce air resistance during driving has become a key path to enhance overall aerodynamic performance and achieve energy-saving and emission-reduction goals. The impact of resistance on a car's appearance during driving is shown in Fig. 1.

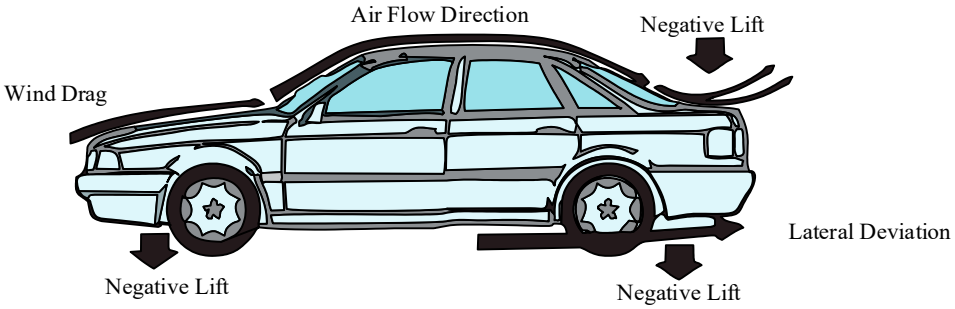

Fig. 1. Resistance distribution of the vehicle during driving

As shown in Fig. 1, the resistance encountered during vehicle operation can be refined into three types of forces: along the direction of travel, lateral displacement, and vertical upward. When the vehicle's speed exceeds 60 kilometers per hour, aerodynamic resistance increases significantly, significantly affecting the vehicle's performance. It is crucial to finely adjust and optimize various aerodynamic design parameters to effectively mitigate the impact of air resistance on vehicles at high speeds (Mondal and Goswami, 2024). The EGO algorithm, due to its high efficiency and accuracy, can finely adjust design parameters. Based on this algorithm, the Kriging surrogate model is used for optimization to accurately guide the design process, find the optimal aerodynamic shape, improve the vehicle's overall driving efficiency and stability, and maximize energy-saving effects (Lizarribar et al., 2024). The improved EGO algorithm structure of the Kriging surrogate model is shown in Fig. 2.

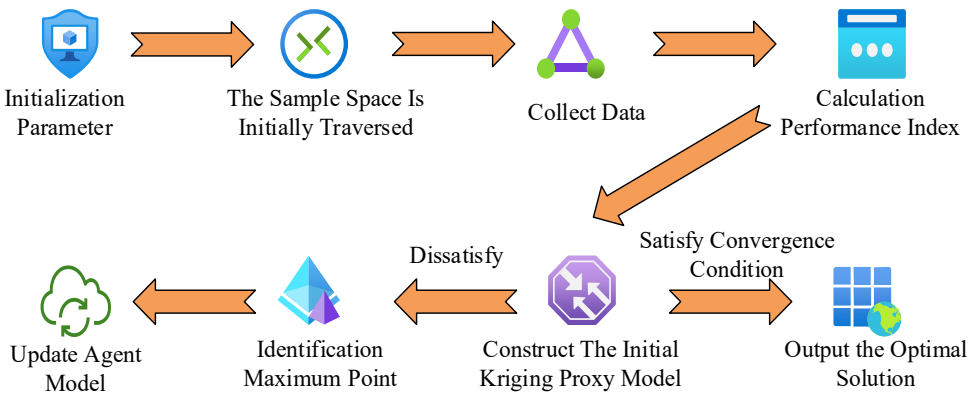

Fig. 2. EGO algorithm structure improved by kriging surrogate model

As shown in Fig. 2, the algorithm first initializes the parameters and then employs an experimental design strategy to traverse the sample space and collect preliminary data. Subsequently, based on the collected sample points, the actual performance indicators are calculated, and an initial Kriging surrogate model is constructed to approximate the true function behavior. A convergence criterion is established as the termination condition for iteration. If convergence is not achieved, use sub-optimization techniques to identify the point with the maximum Expected Improvement (EI) in the current Kriging model, enrich the sample set by evaluating its true performance, and update the surrogate model accordingly to improve prediction accuracy (Wang et al., 2024). The above process is repeated until the preset convergence conditions are met, thus efficiently completing the optimization of aerodynamic appearance design. The study collected samples at different points and obtained their output values. Based on these sample data, the Kriging model is used to calculate the EI function, as shown in Eq. (1).

$$F_{EI} = E\left(vR_g^{n+1} - vR_g^n\right) \tag{1}$$

In Eq. (1), F_{EI} represents the EI function, E represents the expected operation, v represents integration, and R_g^{n+1} represents the dataset observed in the $n+1$ th iteration. By using partial integration, the study adopts a closed-form expression for EI, as shown in Eq. (2).

$$E[I(x)] = \left(f_{\min} - \mu(x)\right)\Phi\left(\frac{f_{\min} - \mu(x)}{\sigma(x)}\right) + \sigma(x)\phi\left(\frac{f_{\min} - \mu(x)}{\sigma(x)}\right) \tag{2}$$

In Eq. (2), $\left(\mu(x), \sigma^2(x)\right)$ represents the upper and lower limits of the function distribution, $E[I(x)]$ represents the EI value, $f_{\min}$ represents the minimum response value, Φ represents the cumulative density, and ϕ represents the probability density. The calculation method of the probability density function is represented in Eq. (3) (Chen et al., 2024).

$$\phi(x) = \frac{1}{\sqrt{2\pi}\sigma(x)}\exp\left(-\frac{1}{2}\left(\frac{K(x) - \mu(x)}{\sigma(x)}\right)^2\right), K(x) \in \left(\mu(x), \sigma^2(x)\right) \tag{3}$$

In Eq. (3), $K(x)$ is the predicted value of the Kriging surrogate model, and the calculation method for the next sampling point is shown in Eq. (4).

$$x_{n+1} = \arg\max_x E[I(x)] \tag{4}$$

In Eq. (4), x represents the sampling point and $\arg$ represents the average value. The calculation method of Kriging surrogate model is shown in Eq. (5).

$$K(x) = \sum_{d=1}^{k} \alpha_d M_d(x) + S(x) \tag{5}$$

In Eq. (5), α_d represents the corresponding coefficient, M_d represents the regression module, $S(x)$ represents the random function, and the average is 0. The covariance matrix calculation method for each point in $S(x)$ is shown in Eq. (6).

$$J\left[S\left(x^a\right), S\left(x^b\right)\right] = \delta^2 J_r\left[J_r\left(x^a, x^b\right)\right] \tag{6}$$

In Eq. (6), $J\left[S\left(x^a\right), S\left(x^b\right)\right]$ represents the covariance matrix of the random function for design points a and b, δ^2 means the variance of the random function, and J_r means the correlation matrix with mirrored features. The calculation method for J_r is shown in Eq. (7).

$$\begin{cases} J_r\left(x^a, x^b\right) = \prod_{k=1}^{d} \exp\left(-\sigma_k \left|x_k^a - x_k^b\right|^{g_k}\right) \\ \sigma_k \geq 0 \\ 0 \leq g_k \leq 2 \end{cases} \tag{7}$$

In Eq. (7), $J_r\left(x^a, x^b\right)$ represents the correlation matrix between design points a and b, $\prod$ represents the multiplication operation of each term, σ_k represents the nonlinear characteristics of the correlation matrix in the k th coordinate system, and g_k represents the sliding value of the correlation matrix in the k th coordinate system. When

$g_k = 2$, the correlation matrix is a smooth matrix. After determining the nonlinear features and sliding values, the calculation method for the predicted value at the sampling point is given by Eq. (8) (Nguyen, 2024).

$$C(x) = \overline{\alpha} + L(x) \times \frac{1}{g_k} \times \frac{\alpha}{c} \tag{8}$$

In Eq. (8), $C(x)$ represents the predicted value at sampling point x, α means the predicted average value, $\overline{\alpha}$ represents the result of performing a generalized least squares operation on α, $L(x)$ represents the correlation matrix between sampling point x and other sampling points, and c represents the response value of the sampling point. The operation process of $\overline{\alpha}$ is shown in Eq. (9).

$$\overline{\alpha} = \frac{1}{g_k} \times \frac{c}{g_k} \tag{9}$$

The calculation method for the mean square error of the predicted value $C(x)$ at the sampling point x is shown in Eq. (10).

$$MSE\left[C(x)\right] = \delta^2 \left[1 - \begin{pmatrix} 1 \\ L(x) \end{pmatrix}^T \begin{pmatrix} 0 & 1^T \\ 1 & g_x \end{pmatrix} \begin{pmatrix} 1 \\ L(x) \end{pmatrix}\right] \tag{10}$$

In Eq. (10), $MSE\left[C(x)\right]$ represents the mean square error of the predicted value $C(x)$ at sampling point x, and T represents the transpose of the matrix. In optimization exploration, the EI function exhibits an adaptive mechanism, that is, when the predicted point estimation value is low or the estimation precision of the model is limited, the EI function will automatically increase the EI value of the corresponding region as a guide, prompting the optimization process to focus on these potential high return regions in order to achieve significant improvement effects (Dini et al., 2024). Research will combine the EGO algorithm with the local optimization algorithm to improve optimization efficiency. When the EGO algorithm approaches convergence, the Broyden-Fletcher-Goldfarb-Shanno Algorithm (BFGS) is used to continue the search, reducing the surrogate model's error and seeking a more accurate and optimal solution (Sait et al., 2025). The BFGS algorithm effectively leverages gradient information to accelerate convergence and flexibly handle complex problems. The BFGS algorithm process is shown in Fig. 3.

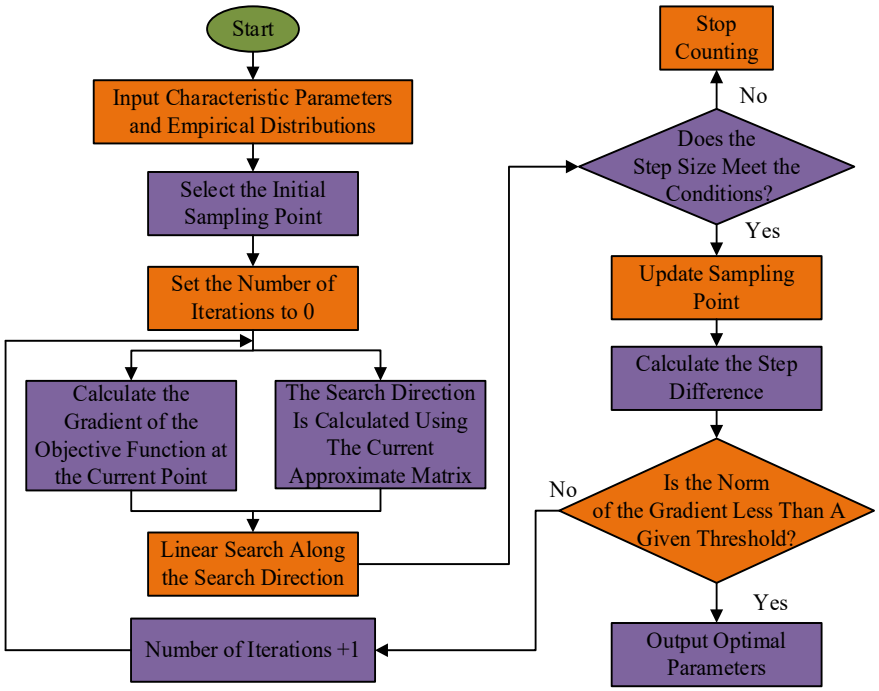

Fig. 3. BFGS algorithm flow chart

In Fig. 3, the BFGS algorithm gradually constructs an approximate inverse of the Hessian matrix through an iterative

optimization strategy, effectively bypassing the need to directly compute complex Hessian matrices and significantly reducing the computational burden. The calculation method of the Hessian matrix is represented in Eq. (11).

$$H_{ab} = \frac{f(x+\lambda e_a+\lambda e_b)-f(x+\lambda e_a)-f(x+\lambda e_b)+f(x)}{\lambda^2} \tag{11}$$

In Eq. (11), H_{ab} represents the Hessian matrix at coordinate position (a,b), e_a and represents the unit vectors in different directions, λ is a smaller constant, and $f(x)$ represents the function operation. Compared to gradient descent, BFGS converges faster because it can intelligently adjust the search direction (Yin et al., 2024). The Broyden-Fletcher-Goldfarb-Shanno Efficient Global Optimization (BF-EGO) algorithm combines the BFGS and EGO algorithms. The BF-EGO algorithm has excellent numerical and stability properties, and is suitable for handling optimization problems in high-dimensional spaces. It can stably and efficiently lead to optimal solutions.

2.2. Establishing an Optimization Model for Automotive Pneumatic Appearance Design

After successfully integrating the local optimization efficiency of the BFGS algorithm with the global exploration ability of the EGO algorithm, the BF-EGO algorithm was constructed. The study applied the BF-EGO algorithm to the complex field of automotive aerodynamic design, aiming to further improve automobile aerodynamic performance and achieve design optimization through accurate, robust algorithmic models (Yue et al., 2024). To ensure consistency in experimental verification, a car simulation model was used in the study to optimize aerodynamic performance. The car simulation experimental model is shown in Fig. 4.

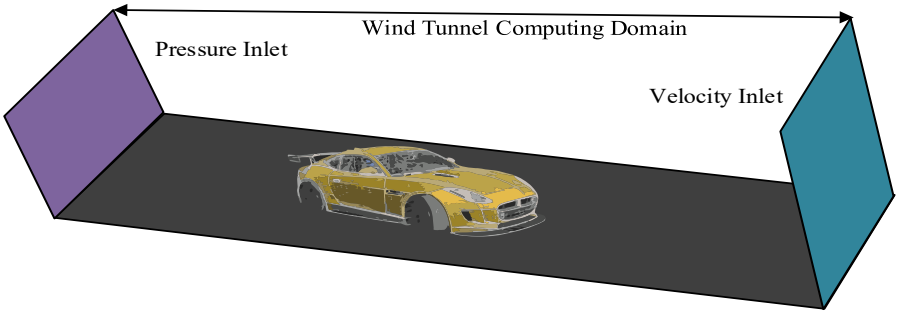

Fig. 4. Automobile simulation experiment model

As shown in Fig. 4, due to limited computing resources, a finite-size calculation area was set up to perform the simulation analysis. The calculation area is rectangular, and its boundary conditions are carefully designed to ensure the rationality and accuracy of the optimization results. Specifically, the distance between the vehicle's front end and the boundary of the simulated area entrance is three times the vehicle's length, aiming to reduce the potential impact of entrance effects on the simulation of the vehicle flow field. At the same time, the distance from the rear of the vehicle to the exit boundary is set to 4 times the vehicle's length to fully capture the vehicle's features.

Additionally, in the width direction, the width of the entire calculation area is set to 7 times the vehicle width, and the distance between the vehicle and the area's side walls is kept at 3 times the vehicle width. This layout helps ensure accurate simulation of crosswind effects and lateral flow around the vehicle. In terms of height, based on the vehicle's actual size and driving environment, the calculation area is set to 5 times the vehicle's height. To better reflect the real situation and avoid convergence issues during the calculation, the model has slightly flattened the front and rear wheels and, accordingly, raised the bottom of the calculation area by 0.05 meters, while removing modules below the bottom. This adjustment helps to more accurately reflect the interaction and flow details between the wheels and the ground. The different surface grids of vehicles have varying degrees of influence on aerodynamics. To reduce the aerodynamic impact, the surface grids of each vehicle part are unified into triangles, as shown in Fig. 5.

As shown in Fig. 5, the overall grid layout ensures the absence of free boundaries and repetitive elements and adopts a refined partitioning strategy. In terms of surface mesh design, a highly adaptable sectional mesh technology was selected, with a maximum cell size set at 500 millimeters to optimize computational efficiency and accuracy. For the boundary layer, a prism-layer mesh model was specifically used, with no additional boundary layer applied on the periphery of the computational domain, focusing on the vehicle body. Five layers of fine boundary layers were set, each with a thickness of 10 millimeters and a constant growth rate of 1. Based on past practice, areas such as the tail wing, rearview mirrors, body, and sunroof are considered critical areas due to the complexity of airflow. To this end, in the STAR-CCM+software, research is being conducted on the use of custom control functions to create targeted volume mesh encryption areas (Liu et al., 2024). This strategy improves the accuracy of gas behavior in complex flow regions during simulation by locally encrypting the grid, thereby more accurately capturing and predicting the dynamic changes in gas flow in these key areas. After dividing the aerodynamic calculation area into various surface grids, it is necessary to specify the basic aerodynamic parameters. The calculation method of characteristic length in turbulence parameters is shown in Eq. (12).

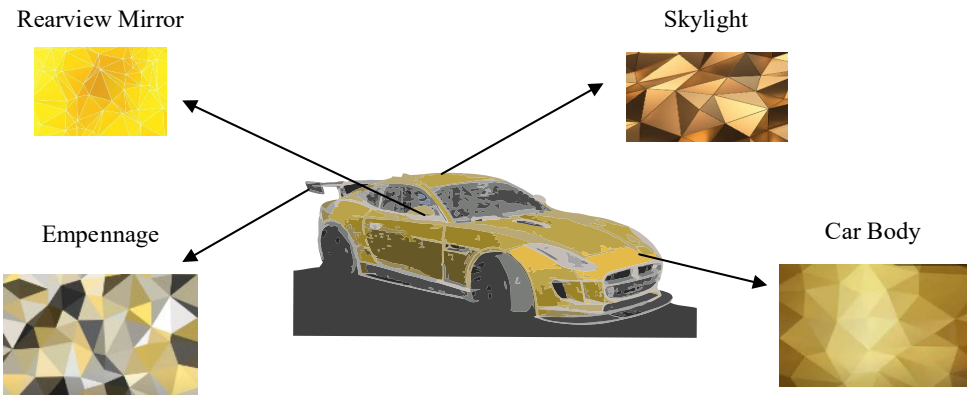

Fig. 5. Grid diagram of each part of the vehicle

$$T_d = 2\sqrt{\frac{g_{in} \times k_{in}}{\pi}} \tag{12}$$

In Eq. (12), T_d represents the feature length, g_{in} represents the height of the entrance edge, and k_{in} represents the width of the entrance edge. The calculation method of turbulence scale is shown in Eq. (13) (Sonko et al., 2024).

$$C_d = 0.07T_d = 0.14\sqrt{\frac{g_{in} \times k_{in}}{\pi}} \tag{13}$$

The calculation method for turbulence intensity is shown in Eq. (14) (Mehta, 2024).

$$Q_d = 0.16\,\mathrm{Re}^{-\frac{1}{8}} \tag{14}$$

In Eq. (14), Q_d represents turbulence intensity and Re represents the Reynolds coefficient. The calculation method for Re is shown in Eq. (15).

$$\mathrm{Re} = \frac{A_\rho A_v C_d}{A_\mu} \tag{15}$$

In Eq. (15), A_ρ represents air density, A_μ represents the viscosity coefficient of air, and A_v represents airflow velocity. To accurately optimize the aerodynamic appearance design, the wind tunnel structure used to obtain the aerodynamic parameter model is shown in Fig. 6.

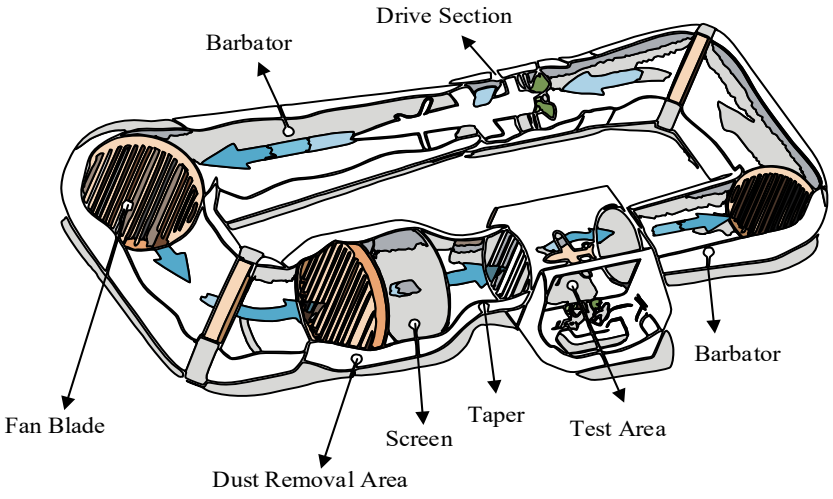

Fig. 6. Schematic diagram of wind tunnel structure

As shown in Fig. 6, this wind tunnel employs a reflux design with a maximum wind speed of 80m/s, meeting the needs of various high-speed flow tests. The wind speed measurement system built into the model can accurately adjust wind speed under various complex operating conditions, enabling real-time control. The model is also equipped with a high-precision six-directional force balance system, which can capture the six-directional forces acting on the test model in real time and accurately, providing real-time and accurate mechanical data. In addition, the study used laser particle velocimetry to monitor the fluid flow details around the model in real time, providing rich visualization information for the parameters of the airflow in all directions and ensuring data accuracy. To simulate the ground effect more realistically, a mobile belt device was installed to effectively eliminate the adverse effects of the ground surface layer on the experimental results and improve the accuracy of parameter optimization. Finally, the model's parameters are used to optimize and adjust the appearance of various parts of the vehicle.

3. Results

3.1. Effects of Automotive Pneumatic Experiments

To ensure the accuracy of the aerodynamic simulation experiment, the operating system used for the simulation was Windows 11, the programming language was Python 3.8, the CPU was an Intel Core i5-12600K @ 4.90 GHz, the GPU was a GeForce RTX 4060Ti, and the memory was 32GB. The experimental data of two different appearance cars in the wind tunnel model mainly included the drag coefficient (DC), calculated residual (CR), and pressure situation (PS). The drag coefficient of the car under different wind speeds is shown in Fig. 7.

According to Fig. 7(a), the drag coefficient of car 1 decreased with increasing wind speed during testing. Due to the relative speed, a wind speed of 60km/h was equivalent to a car traveling at 60km/h in a windless state. The speed limit on urban roads was generally 60km/h, while the speed limit on highways was generally 120km/h. In the actual simulation process, after optimizing the car parameters using the BF-EGO algorithm, the car could adaptively adjust its appearance, such as sunroof opening and closing, according to the actual wind speed, resulting in an overall decrease in the car's resistance coefficient, which was an average decrease of 36.89% compared to before optimization. When the wind speed was 60km/h, the drag coefficient of car 1 was 0.404, and when the wind speed was 120km/h, the drag coefficient of car 1 was 0.384. As shown in Fig. 7(b), car 2 with a lower body had a lower drag coefficient when the wind speed was higher. When the wind speed was 60km/h, the drag coefficient of car 2 was 0.404, and when the wind speed was 120km/h, the drag coefficient of car 2 was 0.379. From this, it can be seen that after optimizing the car parameters using the BF-EGO algorithm, the overall resistance coefficient during driving decreased. Vehicles with lower body height had lower drag coefficients at high speeds, but this effect was not significant at lower speeds. The observation and calculation residuals of the drag coefficient are shown in Fig. 8.

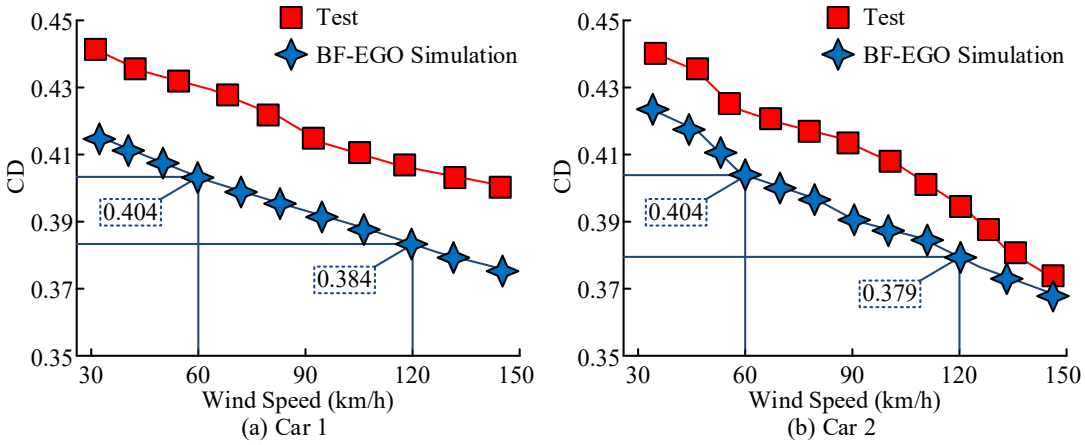

Fig. 7. The Drag Coefficient of the Car at Different Wind Speeds

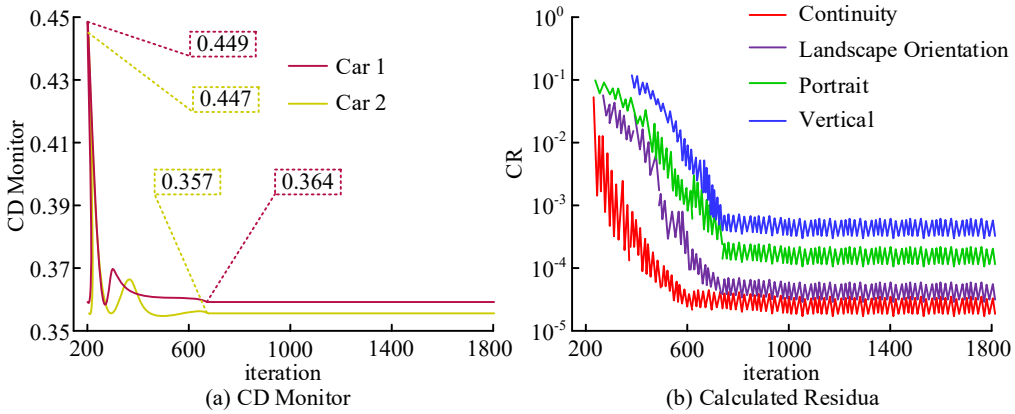

Fig. 8. Resistance coefficient monitoring chart and calculated residual chart

From Fig. 8(a), it can be seen that the drag coefficients for cars 1 and 2 were similar. When the number of iterations was 200, the highest observed drag coefficient was 0.449 for car 1 and 0.447 for car 2. The resistance coefficient tended to stabilize at 400 iterations and ultimately settled between 0.357 and 0.364. From Fig. 8(b), it is told that the calculated residuals of the car in all directions stabilized and oscillated below 10-3 when the iteration number reached 720, and the continuously calculated residuals were as low as 6×10^{-5}. Therefore, the data obtained by the BF-EGO algorithm showed good convergence and met the indicators required for appearance design. To more intuitively demonstrate the car's position during the wind tunnel experiment, the pressure and environmental velocity cloud maps of the car's surface are shown in Fig. 9.

As shown in Fig. 9(a), the front end and tire section of the car were subjected to the highest pressure, reaching 486 Pa. This was because during the driving process of a car, the front end of the vehicle came into direct contact with the air and produced an interaction, which caused some of the vehicle's kinetic energy to be converted into potential energy, thus creating a positive pressure zone in the front area of the car. As shown in Fig. 9(b), during vehicle operation, the airflow on the surface of the vehicle underwent complex changes, especially on the sides, roof, sunroof, and rear of the vehicle, where airflow separation was significant, forming negative pressure zones. The airflow velocity at the intersection of the intake grille, hood, and windshield was relatively high. The average speed was 121km/h, and the exhaust flow of the vehicle belongs to the key area where it was easy to detach from the body, with a relative airflow velocity of 0. Therefore, vehicle aerodynamic optimization mainly involved improving the appearance of the front and roof parts.

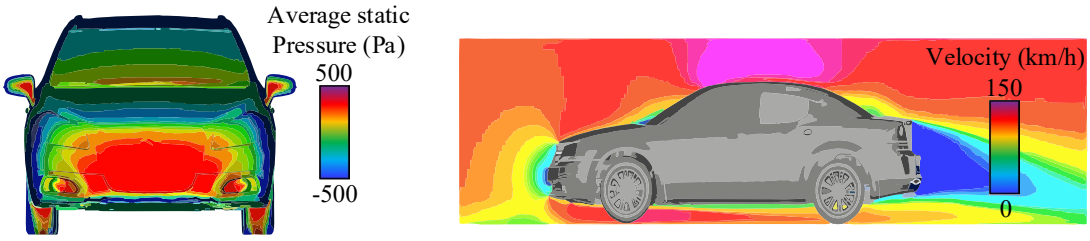

(a) Pressure Distribution Cloud Picture (b) Velocity Distribution Cloud Picture

Fig. 9. A Cloud image of the surface pressure and wind speed of a car

3.2. Comparison of Algorithm Performance

After conducting an in-depth analysis of automotive aerodynamic simulation experiments, this study compares the performance of different steering algorithms to explore their advantages and disadvantages in simulating and predicting automotive aerodynamic performance. The comparative algorithms are the traditional EGO algorithm and the second-generation Non-dominated Sorting Genetic Algorithms (NSGA-II). The performance evaluation indicators include prediction error, changes in vehicle resistance, and energy consumption. The prediction errors of the different algorithms during the experiment and verification processes are shown in Fig. 10.

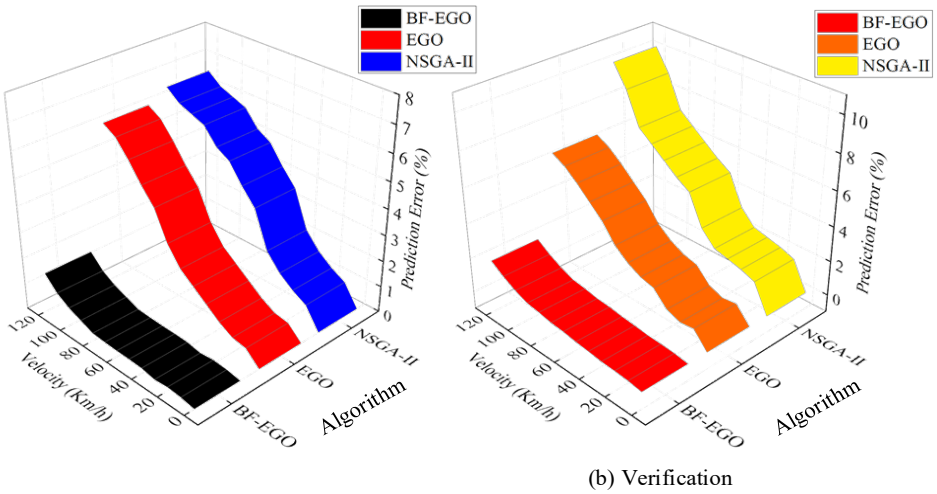

(b) Verification

Fig. 10. Prediction error of different algorithms in experiment and verification

As shown in Fig. 10(a), during the testing phase, the prediction error of the BF-EGO algorithm was the smallest. Due to the influence of the BFGS algorithm, the BF-EGO algorithm could maintain high prediction accuracy even at high speeds, with a maximum prediction error of 1.5%. The EGO and NSGA-II algorithms yielded similar results, and as speed increased, the prediction error grew larger. As shown in Fig. 10(b), during verification, the prediction errors of each algorithm increased slightly due to environmental factors. The BF-EGO algorithm had the least impact, with a maximum prediction error of 2.1%, while the NSGA-II algorithm had a maximum prediction error of over 10%. Therefore, the BF-

EGO algorithm achieved higher prediction accuracy, with a prediction error of less than 5%, meeting conventional requirements. After preliminary optimization of the car's appearance, the changes in resistance of various parts of the car are represented in Table 1.

Table 1. The resistance changes of various parts of the car

Resistance (Pa)	Before optimization	BF-EGO	EGO	NSGA-II
Vehicle front end	486	478	481	483
Vehicle rear-view mirror	458	398	428	435
Top of vehicle	101	56	95	98
Front windshield of vehicle	312	261	289	292

According to Table 1, the resistance experienced by the vehicle was mainly concentrated at the front end and rearview mirror. After preliminary appearance optimization using different algorithms, the BF-EGO algorithm achieved the best optimization results. The BF-EGO algorithm reduced the front-end resistance from 486 Pa to 478 Pa by changing the design of the intake grille, reducing it by 1.65%. Due to the need to consider engine intake at the front end of the car, resistance could not be further reduced. The BF-EGO algorithm optimized the shape of the car rearview mirror, the material of the front windshield, and the flatness of the roof sunroof, further reducing the overall resistance, with the most significant reduction of 44.56% in the sunroof section. The optimization of other algorithms was poor. This shows that using the BF-EGO algorithm to optimize a car's aerodynamic appearance can significantly reduce the vehicle's overall drag. The fuel consumption per 100 kilometers after aerodynamic optimization of the vehicle using different algorithms is shown in Fig. 11.

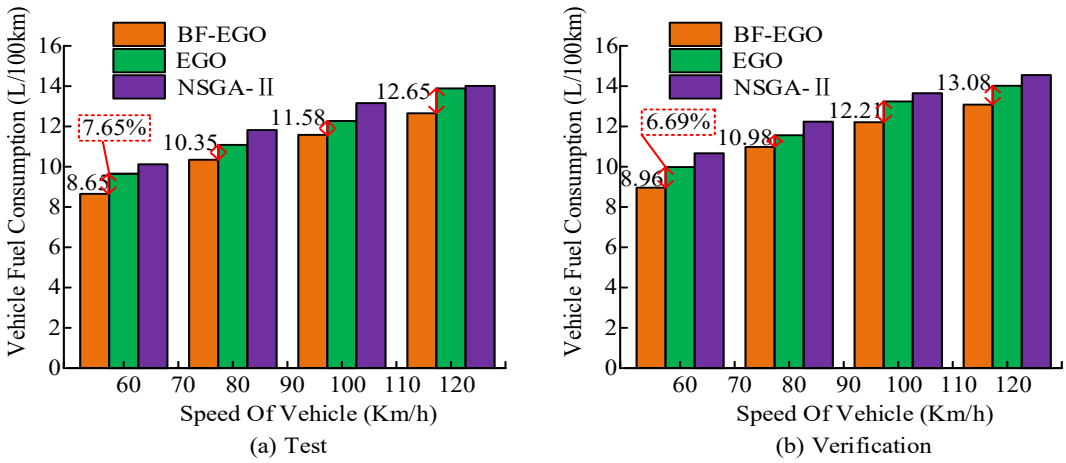

Fig. 11. Fuel consumption of 100 km after vehicle optimization

As shown in Fig. 11(a), the fuel consumption per 100 kilometers of a vehicle was greatly affected by its speed. The higher the vehicle speed, the higher the relative fuel consumption. During testing, the optimized BF-EGO algorithm achieved a fuel consumption of 8.65 L/100 km at 60 km/h, which was 7.65% lower than the second EGO algorithm. From Fig. 11(b), it is evident that the car's fuel consumption during actual driving was higher than the ideal fuel consumption during testing. This was because the actual driving speed was not always constant, and could only maintain the final average speed to meet the requirements. In actual driving, the BF-EGO algorithm optimized car still had the best energy consumption, with a fuel consumption of 8.96L per 100 kilometers at a speed of 60Km/h, which was 6.69% lower than the second EGO algorithm. In summary, the BF-EGO algorithm had the best aerodynamic appearance design optimization performance and outperformed other traditional algorithms in various experimental indicators.

To address the gap between numerical optimization performance and real-world automotive design practice, it is necessary to clarify how the proposed BF-EGO algorithm can be embedded into practical aerodynamic design workflows. In industrial vehicle development, exterior aerodynamic optimization is typically an iterative process involving repeated CFD simulations, geometric modifications, and physical or virtual prototyping, resulting in long development cycles and high computational and testing costs. Therefore, beyond numerical accuracy, the practical value of an optimization algorithm lies in its ability to reduce design iterations, shorten optimization cycles, and support engineering decision-making under realistic simulation constraints. To this end, an application-oriented evaluation is conducted to compare the proposed BF-EGO algorithm with the conventional EGO and NSGA-II methods with respect to design efficiency, computational resource consumption, and workflow integration. The results are summarized in Table 2.

Table 2. Practical application comparison of different optimization algorithms in automotive aerodynamic design

Evaluation Aspect	BF-EGO	Traditional EGO	NSGA-II
Average number of CFD iterations to convergence	≈ 400	≈ 650	≈ 900
Average aerodynamic design iterations	5–6	8–9	10–12
Surrogate model prediction error	≤ 2.1%	≤ 5.8%	≥ 10%
CFD computation time per optimization cycle	Reduced by ~35%	Baseline	Increased by ~20%
Physical/virtual prototype redesigns required	1–2	3–4	≥ 4
Integration with CFD software (e.g., STAR-CCM+)	High (direct coupling)	Medium	Medium
Suitability for early-stage styling optimization	High	Medium	Low
Applicable vehicle type	Passenger vehicles (sedan/SUV)	General	General
Simulation environment constraint	Steady-state CFD, wind tunnel validated	Same	Same

According to Table 2, the proposed BF-EGO algorithm provides clear advantages when evaluated from the perspective of real automotive design workflows rather than purely numerical performance. First, in terms of design efficiency, BF-EGO significantly reduces the number of CFD iterations required to reach convergence. Compared with traditional EGO and NSGA-II algorithms, the average convergence iteration count is reduced by approximately 38% and 56%, respectively. This directly translates into fewer geometry modification cycles and faster decision-making during aerodynamic appearance refinement. Second, the improved surrogate model accuracy achieved by combining Kriging with BFGS-based local refinement allows designers to rely more confidently on virtual optimization results. With prediction errors consistently below 2.1%, the need for repeated physical or high-fidelity virtual prototype validation is substantially reduced. In practical development scenarios, this means fewer prototype redesigns and lower development costs, especially in the early styling and concept design stages, where aerodynamic trends are evaluated rather than final certification values. Third, from a workflow-integration perspective, BF-EGO can be seamlessly embedded into existing CFD-driven design environments such as STAR-CCM+. The algorithm operates under standard steady-state aerodynamic simulation settings and does not require additional experimental infrastructure, making it suitable for industrial deployment. However, its application is currently constrained to passenger vehicle configurations under steady driving conditions, and the optimization results are influenced by the fidelity of the CFD model and boundary condition assumptions. Overall, the proposed BF-EGO algorithm not only improves numerical optimization performance but also enhances engineering efficiency by shortening development cycles, reducing computational cost, and supporting iterative design decisions. These characteristics make it particularly valuable for early to mid-stage automotive aerodynamic appearance design, where rapid evaluation and optimization are critical.

4. Conclusion

This study mainly used computer algorithms to optimize the design of automotive aerodynamic appearance. To optimize aerodynamic appearance in different directions, a new BF-EGO algorithm was developed by combining the BFGS and EGO algorithms. The EGO algorithm first initialized the parameters, used the Kriging model for prediction, and then used the BFGS algorithm to obtain the optimal parameters that met the preset conditions. Finally, a wind tunnel experimental platform was built to test the optimized vehicle. The research results showed that after optimizing the car parameters using the BF-EGO algorithm, the overall drag coefficient decreased by an average of 36.89% compared to before the pre-optimization. The resistance coefficient stabilized at 0.364~0.357 when the number of iterations reached 400. In actual operation, the maximum prediction error of the BF-EGO algorithm was 2.1%, which could meet the requirement of an error below 5%. The BF-EGO algorithm reduced the front-end resistance from 486 Pa to 478 Pa, resulting in a 1.65% decrease and a 44.56% decrease in sunroof resistance. During actual driving, the BF-EGO algorithm optimized the car's fuel consumption per 100 kilometers at a speed of 60Km/h to 8.96L, which was 6.69% lower than the second EGO algorithm. In summary, the BF-EGO algorithm not only achieved high prediction accuracy and precision but also exhibited fast convergence. After aerodynamic optimization, the wind resistance of the car's various parts was significantly reduced, thereby reducing energy consumption. Although this study solved the optimization problems of automotive aerodynamic appearance and energy consumption, it did not conduct in-depth research on optimization beyond appearance, such as vehicle structure. Further exploration of automotive structural optimization should be conducted in the future.

Author Contributions

Zhonghua Zhao contributes to conceptualization, methodology, analysis, manuscript editing, and funding acquisition. Zhibin Qiu contributes to validation, data collection, and manuscript editing.

Funding

The research is supported by: 2023 Young and Middle-aged Faculty Action Program in Universities: Discipline (Specialty) Leader Cultivation Project, (NO. DTR2023098). 2024 Provincial Higher Education Quality Engineering Project, Specialized Programs (Micro-majors) Serving the Ten Emerging Industries; Cultural Product Creative Design, (NO. 2024cywzy096).

Institutional Review Board Statement

Not applicable.

References

Amirkhani, A., Shirzadeh, M., and Heydari, J. (2024). Automotive electric power steering control with robust observer based neuroadaptive type-2 radial basis function methodology. *IEEE Open Journal of Vehicular Technology,* 5(1), 592-605.

Chen, Z., Biggie, H., Ahmed, N., Julier, S., and Heckman, C. (2024). Kalman filter auto-tuning with consistent and robust Bayesian optimization. *IEEE Transactions on Aerospace and Electronic Systems,* 60(2), 2236-2250.

Dini, P., Basso, G., Saponara, S., and Romano, C. (2024). Real-time monitoring and ageing detection algorithm design with application on SiC-based automotive power drive system. *IET Power Electronics,* 17(6), 690-710.

Hossain, M., Rahman, M., and Ramasamy, D. (2024). Artificial intelligence-driven vehicle fault diagnosis to revolutionize automotive maintenance: A review. *Computer Modeling in Engineering & Sciences*, 141(2), 951-952.

Huynh, T., Pham, T., Lee, J., and Nguyen-Xuan, H. (2024). Optimal parametric design of fuel cell hybrid electric vehicles by balancing composite motion optimization. International *Journal of Precision Engineering and Manufacturing-Green Technology,* 11(1), 123-143.

Liu, C. (2024). Energy consumption prediction and optimization of electric vehicles based on RLS and Improved SOA. *IEEE Access,* 12(1), 38180-38191.

Liu, L., and Calderon, D. (2024). Optimization design of air filter housing structure based on computational fluid dynamics. *In Third International Conference on Advanced Manufacturing Technology and Electronic Information* (AMTEI 2023), 13081(1), 77-82.

Liu, R., Xiao, D., Lin, D., and Zhang, W. (2024). Intelligent bearing anomaly detection for industrial Internet of Things based on auto-encoder Wasserstein generative adversarial network. *IEEE Internet of Things Journal,* 11(13), 22869-22879.

Lizarribar, B., Prieto, B., Selema, A., Ibrahim, N., Sergeant, P., Artetxe, G., and Martinez-Iturralde, M. (2024). Multiphysics Topology Optimization of Aluminum and Copper Conductors for Automotive Electrical Machines. *IEEE Transactions on Transportation Electrification,* 10(4), 9342-9350.

Mehta, P., Yildiz, S., Sait, M., and Yıldız, R. (2024). Optimization of electric vehicle design problems using improved electric eel foraging optimization algorithm. *Materials Testing,* 66(8), 1230-1240.

Mondal, S., and Goswami, S. (2024). Machine learning applications in automotive engineering: Enhancing vehicle safety and performance. *Journal of process management and new technologies,* 12(1-2), 61-71.

Nainggolan, N., Maghsoudlou, E., AlWadi, M., Atamurotov, F., Kosov, M., and Putra, W. (2024). Advancements in optimization for automotive manufacturing: Hybrid approaches and machine learning. *International Journal of Industrial Engineering and Management,* 15(3), 254-263.

Nguyen, T. A. (2024). Development of a novel integrated control strategy for automotive electric power steering systems. *IEEE Transactions on Automation Science and Engineering,* 22(1), 926-943.

Sait, M., Mehta, P., Pholdee, N., Yıldız, S., and Yıldız, R. (2024). Artificial neural network infused quasi oppositional learning partial reinforcement algorithm for structural design optimization of vehicle suspension components. *Materials Testing,* 66(11), 1855-1863.

Sonko, S., Daudu, D., Osasona, F., Monebi, M., Etukudoh, A., and Atadoga, A. (2024). The evolution of embedded systems in automotive industry: A global review. *World Journal of Advanced Research and Reviews,* 21(2), 96-104.

Wang, H., Wang, Z., Fan, Y., Gao, Q., and Wang, H. (2024). Multi-objective lightweight design of automotive battery pack box for crashworthiness. *International Journal of Crashworthiness*, 29(2), 292-307.

Wang, X. (2025). Draco lizard optimizer: a novel metaheuristic algorithm for global optimization problems. *Evolutionary Intelligence*, 18(1), 10-11.

Xia, Z., and Huang, M. (2024). Optimizing the Aerodynamic Efficiency of Electric Vehicles via Streamlined Design: A Computational Fluid Dynamics Approach. *International Journal of Heat & Technology,* 42(3), 865-866.

Yin, S., Li, H., Laghari, A., Gadekallu, T. R., Sampedro, A., and Almadhor, A. (2024). Anomaly detection model based on deep auto-encoder and capsule graph convolution via sparrow search algorithm in 6G Internet of Everything. *IEEE Internet of Things Journal,* 11(18), 29402-29411.

Yue, M., Zhang, X., Teng, T., Meng, J., and Pahon, E. (2024). Recursive performance prediction of automotive fuel cell based on conditional time series forecasting with convolutional neural network. *International Journal of Hydrogen Energy,* 56(1), 248-258.

Zhonghua Zhao is an associate professor at Anhui Business and Technology College. He graduated from Wuhan University of Technology, China. His research areas include design art, product art design, and visual communication design. He has published more than 10 papers and two books.

Zhibin Qiu is an associate professor at Anhui Business and Technology College. He received a Ph.D. in Design from Hanseo University, South Korea. His research fields include design art, space design, and visual communication design. He has published more than 10 papers.